# IMPACT OF FUSELAGE CROSS SECTION ON THE STABILITY OF A GENERIC FIGHTER

Robert M. Hall†
NASA Langley Research Center
Hampton, Virginia

## ABSTRACT

Many traditional data bases, which involved smooth-sided forebodies, are no longer relevant for designing advanced aircraft. The current work provides data on the impact of chined-shaped fuselage cross section on the stability of a generic fighter configuration. Two different chined-shaped fuselages were tested upright and inverted. It was found that a fuselage with a 30° included chine angle resulted in significantly higher values of $C_{L,max}$ than a fuselage with a 100° included chine angle. This difference was attributed to the more beneficial vortical interaction between the stronger forebody vortices coming off of the sharper chine edges and the wing vortices. The longitudinal stability of the configuration with the sharper chine angle was also better because, based on pressures and flow visualization, the vortex burst over the wing was delayed until significantly higher values of $\alpha$. Unstable rolling moment derivatives were also delayed to higher values of $\alpha$ for the sharper chine angle cross section. Furthermore, it was found that directional stability of both of the upright configurations, which had larger lofts in cross section above the chine lines than below the chine lines, was better than for the inverted configurations.

## INTRODUCTION

Current advanced fighter designs usually include a fuselage with chine-shaped cross section to minimize observables. The presence of the chines results in a fixed location of flow separation and generally stronger forebody vortices being shed than would be the case for a configuration with a smooth-sided forebody. These stronger vortices can be useful in that they can synergistically augment the lift over the main wing; however, these chine vortices can also lead to pitch up and nonlinearities in lateral stability due to windward vortex burst at sideslip. Consequently, vortices from chined forebodies can have a significant impact on both longitudinal and lateral/directional stability.

The present paper describes a portion of a joint NASA and U. S. Air Force study undertaken at the Langley Research Center to investigate the impact of chine-shaped fuselage cross section on the

longitudinal and lateral/directional stability of a generic fighter model. The overall study involved a number of wind tunnel entries at subsonic and transonic speeds. A total of 4 different fuselage cross sections were evaluated. Two of these four fuselages were tested inverted. The 4 fuselages were tested with either a centerline vertical tail, twin vertical tails, or no tails. All the fuselages had the same planform and utilized the same cropped delta wing with a 60° leading-edge sweep. The wing itself was fitted with leading-edge flaps. The test facility, the Langley 7- by 10-Foot High Speed Tunnel (HST), permitted testing to an angle of attack of up to 50° and with sideslip values as large as ±15°. Mach number in this facility was, for the purposes of this test, limited to 0.4. For the present paper, data from the 7- by 10-Foot HST will be reported for two of the fuselage cross sections, each tested upright and inverted. The data for the configurations with no leading-edge flaps deflections and no vertical tails will be presented.

The data obtained during this experimental program have been extensively used for validation of Euler and Navier-Stokes numerical codes. Example publications utilizing these data for code validation include references 1 to 3. While initial experimental results with one configuration were presented in references 4 and 5, this report will examine the

---

†Senior Aerospace Engineer, Configuration Aerodynamics Branch, Associate Fellow, AIAA

impact of changing the shape of the fuselage cross section on the vehicle stability.

## NOMENCLATURE

The longitudinal data are referred to the stability-axis system and the lateral-directional data are referred to the body-axis system. The data are normalized by the usual quantities, such as planform area, span of the wing, and the wing mean aerodynamic chord. The moment reference center was located at the 0.25 mean aerodynamic chord location, which was at model fuselage station 20.36 inches.

$b$     reference wing span, 19.20 in

$C_A$     body-axis axial force coefficient, $\dfrac{\text{Axial Force}}{q_\infty S}$

$C_D$     stability-axis drag coefficient, $\dfrac{\text{Drag}}{q_\infty S}$

$C_L$     stability-axis lift coefficient, $\dfrac{\text{Lift}}{q_\infty S}$

$C_{L,max}$     maximum value of $C_L$

$C_l$     body-axis rolling-moment coefficient, $\dfrac{\text{Rolling moment}}{q_\infty S b}$

$C_{l_\beta}$     derivative of $C_l$ with sideslip, $\beta$, per deg

$C_m$     body-axis pitching-moment coefficient, $\dfrac{\text{Pitching moment}}{q_\infty S \bar{c}}$

$C_n$     body-axis yawing-moment coefficient, $\dfrac{\text{Yawing moment}}{q_\infty S b}$

$C_{n_\beta}$     derivative of $C_n$ with sideslip, $\beta$, per deg

$C_Y$     body-axis side force coefficient, $\dfrac{\text{Side force}}{q_\infty S}$

c.g.     center of gravity

$\bar{c}$     wing mean aerodynamic chord, 12.97 in.

$M_\infty$     free-stream Mach number

NASA     National Aeronautics and Space Administration

$q_\infty$     free-stream dynamic pressure, $lb/in^2$

$R\bar{c}$     Reynolds number based on $\bar{c}$

$S$     reference wing area, 208.19 $in^2$

$\alpha$     angle of attack, deg

$\beta$     angle of sideslip, deg

## DESCRIPTION OF WIND TUNNEL AND MODELS

### Wind Tunnel Facility

The NASA Langley Research Center 7- by 10-Foot HST is a continuous-flow, solid-wall, subsonic/transonic atmospheric wind tunnel, which is described in more detail in reference 6. The model was supported on a sting system with roll positioning capability. A combination of pitch and roll was used to generate the desired combinations of $\alpha$ and $\beta$.

The tunnel was equipped with a laser light sheet capability that was used during the present program to visualize the vortex flow development over the model. This unpublished video record was invaluable in understanding the relationship between the force and moment data, the pressure data, and the complex vortical flow above the model.

### Wind Tunnel Model

The wind tunnel model is shown in schematic form in figure 1. The model has a span of 29.20 inches and a length of 32.48 inches. The wing has a $60^o$ cropped-delta planform incorporating a NACA 65-005 airfoil modified with a double-arc section forward of the maximum thickness and has sharp leading edges. The full-span leading edge flaps are divided into 3 segments of equal span, where only the 2 inner segments were built to be deflected. The model system included options for a centerline vertical tail and twin, wing-mounted vertical tails. A total of 276 static pressure orifices were grouped into six spanwise rows with three on the forebody and three on the wing. The common planform for the two configurations to be reported, which were tested upright and inverted, is shown in figure 2. The model was mounted in the tunnel with a 6-component force and moment balance. For the present report, data for the tails-off configuration with no leading edge flap deflection will be presented.

The fuselage cross-sections are highlighted in figure 3. The two fuselages with total included chine angles of $30^o$ and $100^o$ were run both upright and inverted. Since the wing sections are symmetric top to bottom, running the model inverted highlights the effect of inverting the forebody cross sections, which are not symmetric top to bottom. Details of the fuselage cross sections are included in the following table, where the loft values are the distance

either to the top or bottom of the fuselage from the plane of the chines and is normalized by the local fuselage half width. A photograph of the model with the 30° chine angle installed in the wind tunnel is shown in figure 4.

| Fuselage | Total chine angle | Upper chine angle | Lower chine angle | Loft above chine | Loft below chine |
|---|---|---|---|---|---|
| 1 | 30° | 20° | 10° | 0.75 | 0.5 |
| 2 | 100° | 60° | 40° | 0.75 | 0.5 |
| 1, Inverted | 30° | 10° | 20° | 0.5 | 0.75 |
| 2, Inverted | 100° | 40° | 60° | 0.5 | 0.75 |

RESULTS AND DISCUSSION

The results will be shown for $M_\infty = 0.40$. The figures will present the $\alpha$-polar and $\beta$-polar force and moment data for the fuselages with the 30° (fuselage 1) and 100° (fuselage 2) total included chine angles, upright and inverted, and then calculated $\beta$-derivative data to illustrate the lateral/directional stability of the configurations. The fuselage with the smaller included chine angle, 30°, upright and inverted, is expected to generate stronger chine vortices over the forebody than the fuselage with the 100° chine angle, see reference 7.

Figure 5 shows the $\alpha$-polar data at $\beta = 0°$ for the upright and inverted 30° chine angle configuration. The value of $C_{L,max}$ for the upright configuration is approximately 1.9 and occurs at a value of $\alpha = 38°$. The corresponding value of $C_{L,max}$ for the inverted configuration is about 1.8 and occurs at $\alpha = 35°$. There is no vortex bursting for either the forebody or wing vortices up to $C_{L,max}$, based on the unpublished laser light sheet data. In the plots of $C_L$ versus $C_m$, the curves are very similar, but there is an offset in $C_m$ that may be the result of the change in effective fuselage camber when the fuselage is inverted. As shown in the side view of figure 2, with the higher upper loft of the upright fuselage, a mean fuselage line in side view would have an effective nose droop. Conversely, the inverted fuselage would have an effective nose-up appearance. Consequently, one would expect to see a positive pitch increment when changing from the upright fuselage to inverted fuselage configuration, as indicated. The non-zero values of $C_Y$, $C_l$, and $C_n$ are indicative of asymmetries right to left either in the model geometry or installation or are indicative of asymmetric flow differences.

Figure 6 is the corresponding data for the upright and inverted 100° chine angle configuration. For this configuration, the weaker chine vortices associated with the larger chine angle do not synergistically interact with the wing vortices to the extent that the chine vortices did with fuselage 1. This lack of interaction is evident in the earlier wing vortex burst location both in the flow visualization (not shown) and in the breaks in the lift curve slope at lower values of $\alpha$ for this second fuselage. For this configuration, $C_{L,max}$ is only 1.4 for the upright configuration and 1.5 for the inverted configuration. The respective angles at which vortex bursting occurred are approximately $25°$ and $27.5°$, based on the laser light sheet data, which is why the value of $C_{L,max}$ is lower for the upright configuration. The reason why the inverted configuration had a larger value of $C_{L,max}$ than did the upright configuration while the opposite is true for 30° chine configuration is not known.

Both the upright and inverted 100° chine configurations have a more unstable pitching moment character even at the lower values of $C_L$ than do the upright and inverted configurations with the 30° chine angle. An interesting feature with the two 100° chine configurations is that there are some pronounced lobes in the plots of $C_Y$, $C_l$, and $C_n$ versus $\alpha$ even though the configuration was nominally at $\beta = 0°$. Based on flow visualization and wing pressure data, these lobes correspond to the burst of the wing vortex on one side of the configuration. The beginning of this asymmetric vortex process is most evident in the plot of $C_l$ versus $\alpha$, where it is clear that the vortex asymmetry is occurring concurrently with the breaks in the lift curve slope.

The character of both the 30° and 100° chine angle configurations in sideslip is illustrated in figures 7 and 8. The upright and inverted data for the small chine angle of 30° are shown in figure 7. Significant hysteresis occurs for these configurations in sideslip. In fact, in the figure for $C_l$ versus $\beta$ at $\alpha = 23°$, it can be seen that the data for the upright configuration (circles) are different for negative and positive values of $\beta$. The difference between the data is due to the direction in which $\beta$ was varied. The values of $\beta$ were varied from large negative values to large positive values in one continuous sweep. When the data were repeated later by varying $\beta$ so that the configuration was always going from zero sideslip to larger magnitudes of sideslip, it was found that the character for $C_l$ versus $\beta$ without hysteresis for $\alpha = 23°$ was the one on the positive $\beta$ side of the

curve shown in figure 7. The problem with the negative values of $\beta$ was that the windward vortex system, composed of the chine and wing vortices, was already burst at the higher negative values of $\beta$ and did not reform until $\beta > -2°$. It is the unburst character of the windward chine and wing vortices that give the large negative values of $C_l$ near $\beta = 4°$ for both the upright and inverted configurations. (These upright data at $\alpha = 23°$ are the only $\beta$-polar data which were sampled by a continuous sweep of $\beta$ from negative to positive. All other $\beta$-polars shown were sampled by starting at $\beta = 0°$ and then proceeding to either negative or positive values.)

The trends of the $C_l$ versus $\beta$ plots in figure 7 can be readily explained with the assistance of the laser light sheet data that was simultaneously acquired. For both $\alpha = 23°$ and $30°$, there are clear regions surrounding $\beta = 0°$ that illustrate lateral stability (negative $C_{l_\beta}$). For $\alpha = 23°$, this region is $-4° < \beta < 4°$. For $\alpha = 30°$, this region is $-2° < \beta < 2°$. It is expected that this region may also exist for $\alpha = 35°$, but that it is over such a small range of $\beta$ that it is not evident in the figure. Physically, these regions correspond to the range of $\beta$ where both the windward wing and chine vortices are not burst. At larger magnitudes of $\beta$, the windward chine and wing vortices, which are interacting over the wing, burst and the windward wing loses lift. This results in the large jumps in $C_l$. Note also that while there are laterally stable regions near $\beta = 0°$ for $\alpha = 23°$ and $30°$, the behavior of $C_l$ versus $\beta$ results in regions of lateral stability about non-zero values of $\beta$ at $\alpha = 30°$ and $\alpha = 35°$. For $\alpha = 30°$, the configuration would tend to "fly" near $|\beta| = 5°$ ($C_l = 0$) if it exceeded values of $|\beta|$ greater than $2°$. At $\alpha = 35°$, it may be that any perturbation in sideslip would tend to take the configuration out to $|\beta| = 4°$. At this value of $\alpha$, the configuration may not practically be flyable at $\beta = 0°$ with such a sharp discontinuity in $C_l$ around $\beta = 0°$. With the sharpness of the chine edge in either the upright or inverted orientation, the differences in the strength of the chine vorticity may be relatively small and do not appear to result in significant change to the interactions between the chine and wing vortices.

In figure 7, hysteresis is also responsible for the multiple values of $C_l$ near $\beta = 0°$ at $\alpha = 35°$. These multiple values at $\alpha = 35°$ could be expected to result in multiple values in any $\beta$-derivatives of $C_l$

calculated using values in the neighborhood of $\beta = 0$. That is, in any differencing using the data about $\beta = 0°$, the derivative obtained will vary dramatically depending on whether $C_l = +.04$, 0, or -.04.

The corresponding values of $C_n$ are shown to the right in figure 7 and suggest that the inverted configuration is less directionally stable (stable is defined as $C_{n_\beta}$ positive) for values of $|\beta| > 3°$ for all three values of $\alpha$. This would be expected because the inverted configuration has less side area above the chine line on which the windward chine vortex can act. It is the windward chine vortex which, in sideslip, reduces the pressure on the windward fuselage side (confirmed by unpublished pressure measurements not shown) and is responsible for the restoring moment in $C_n$.

The corresponding $C_l$ data for the fuselage with the $100°$ chine angle is shown in figure 8. For the upright configuration at $\alpha = 23°$, there is no region of local stability around $\beta = 0°$. The inverted configuration does better and exhibits a stable region for $|\beta| < 2°$. Neither the upright or inverted configurations for the $100°$ chine angle fuselage have local regions of stability around $\beta = 0°$ at $\alpha = 30°$ or $35°$. Multiple values in $C_l$ near $\beta = 0°$ are evident at $\alpha = 30°$ and $35°$ for the upright configuration. While there are not multiple values of $C_l$ for the inverted configuration, the fact that the $C_l$ values for $\beta = 0°$ are not near zero for $\alpha = 30°$ and $35°$ suggests the possibility of multiple values if more data had been taken or if the model had been reinstalled in the tunnel.

As was the case for the $30°$ chine configuration, the upright $100°$ chine configuration demonstrates higher restoring moments of $C_n$ over the range of $\beta$ examined. In general, both upright and inverted configurations are stable for $|\beta| < 10°$ with some nonlinearities near $\beta = 0°$.

A more direct look at lateral and directional stability is given in figures 9, 10, and 11. The values of $C_{l_\beta}$ and $C_{n_\beta}$ were calculated by differencing $\alpha$-polars taken at $\beta = -2°$ and $0°$. The value of $\beta = -2°$ was chosen to utilize the large excursions in $C_l$ that occur for all four configurations near this angle of sideslip. The comparisons in figure 9 are for the $30°$ chine angle configurations and are consistent with the observations already made. That is, the lateral stability of the upright and inverted configurations are

very similar. The break in the curves at $\alpha = 30^o$ correlates with the onset of bursting of the wing and chine vortex system over the windward wing for $|\beta| \geq 2°$. In terms of directional stability, the higher levels of directional stability of the upright configuration indicated in figure 7 are again indicated in this plot of $C_{n_\beta}$ versus $\alpha$.

The comparable derivative data for the 100° chine angle configuration is shown in figure 10. For this fuselage cross section, differences occur in $C_{l_\beta}$ between the upright and inverted configurations that are quite pronounced. First, the upright configuration has stable, negative values of $C_{l_\beta}$ over the $\alpha$-range, while the inverted configuration has an unstable region for $25° < \alpha < 31°$. However, as was the case for the 30° chine configuration at $\alpha = 35°$, the values of $C_{l_\beta}$ for the upright 100° configuration could be multivalued at $\alpha = 23°$ because of the multiple values of $C_l$ near $\beta = 0°$, seen in figure 8.

This multivalued nature of the upright 100° configuration is confirmed in figure 11, which repeats the data of figure 10 and adds, for the upright configuration, a second derivative calculation based on another set of $\alpha$-polars at $\beta = 0°$ and -2°. This lack of repeatability makes conclusions difficult regarding the worth of inverting this 100° chine configuration with regard to lateral stability.

As was the case for the 30° configurations, the directional stability of the 100° configuration was slightly better for the upright configuration. Again, this is assumed to be due to the greater area above the chine on which the chine vortex can act.

In comparing the lateral stability of the two fuselages, it appears that the lateral stability of the 100° configuration is not as good as that of the 30° configuration for $\alpha \leq 30°$. However, for $32.5° \leq \alpha \leq 37.5°$, the lateral stability of the 100° configuration appears to be better.

## CONCLUSIONS

An experimental study investigated the impact of forebody cross section geometry on the stability of a generic fighter configuration. It was found that a chined shaped fuselage with the 30° included chine angle (the sharper chine) resulted in significantly higher values of $C_{L,max}$ than a fuselage with a 100° included chine angle. This difference was attributed to the more beneficial vortical

interaction between the stronger forebody vortices coming off of the sharper chine edges and the wing vortices. The longitudinal stability of the sharper chine angle was also better because, based on unpublished pressures and flow visualization, the vortex burst over the wing was delayed until significantly higher values of $\alpha$. Rolling moment derivatives were also much more stable for $\alpha \leq 30°$ for the sharper chine angle cross section. Because of a lack of repeatability, it was inconclusive whether the upright or inverted fuselage orientations gave higher values of lateral stability for either fuselage. Nevertheless, it was found that directional stability of both upright configurations, which had larger lofts in cross section above the chine lines than below the chine lines, was better than for the inverted configurations. The increased directional stability was attributed to the larger side area above the chine on which the windward chine vortex could act. However, the lack of repeatability and the severe nonlinearities in lateral stability for all four configurations would be a significant challenge in developing flight control systems.

## REFERENCES

1. Treiber, David A.; and Muilenburg, Dennis A.: Euler Technology Assessment for Preliminary Aircraft Design Employing OVERFLOW Code With Multiblock Structured-Grid Method. NASA Contractor Report 4651, March 1995.

2. Finley, Dennis B.; and Karman, Steve L., Jr.: Euler Technology Assessment for Preliminary Aircraft Design--Compressibility Predictions by Employing the Cartesian Unstructured Grid SPLITFLOW Code. NASA Contractor Report 4710, March 1996.

3. Kinard, Tom A.; and Raj, Pradeep: Euler Technology Assessment for Preliminary Aircraft Design--Compressibility Predictions by Employing the Unstructured Grid USM3D Code. NASA Contractor Report 4711, March 1996.

4. Rao, Dhanvada M.; and Bhat, M. K.: Subsonic Investigations of Vortex Interaction Control for Enhanced High-Alpha Aerodynamics of a Chine Forebody/Delta Wing Configuration. NASA Contractor Report 189641, June 1992.

5. Rao, Dhanvada M.; and Bhat, M. K.: High-Alpha Vortex Decoupling Investigations on a Chine Forebody/Delta Wing Configuration at Transonic

Mach Numbers.  NASA Contractor Report 189642, June 1992.

6.   Penaranda, Frank E.; and Freda, M. Shannon: *Aeronautical Facilities Catalogue.  Volume I--Wind Tunnels*. NASA RP-1132, 1985.

7.  Nutter, J.:  Leading-Edge Separation from a Thick, Conical, Slender Wing at Small Angles of Incidence.  Journal of Engineering Mathematics, Vol. 15, April 1981, pp. 103-117.
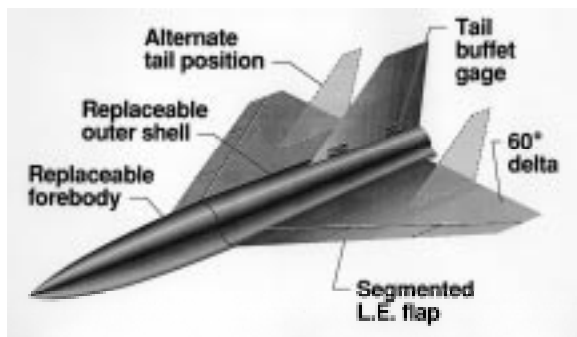


Figure 1.  Schematic of overall model system.
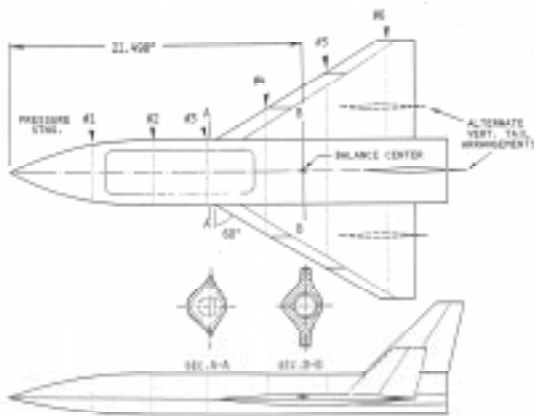


Figure 3.  Schematic of forebody cross sections in the upright orientation.



Figure 2.  Planform and side view of model system.
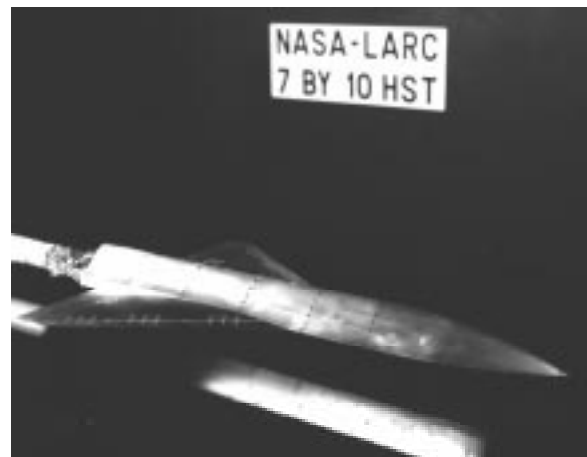


Figure 4.  Installation of 30$^o$ chine angle fuselage configuration in the Langley 7- by 10-Foot HST.

American Institute of Aeronautics and Astronautics

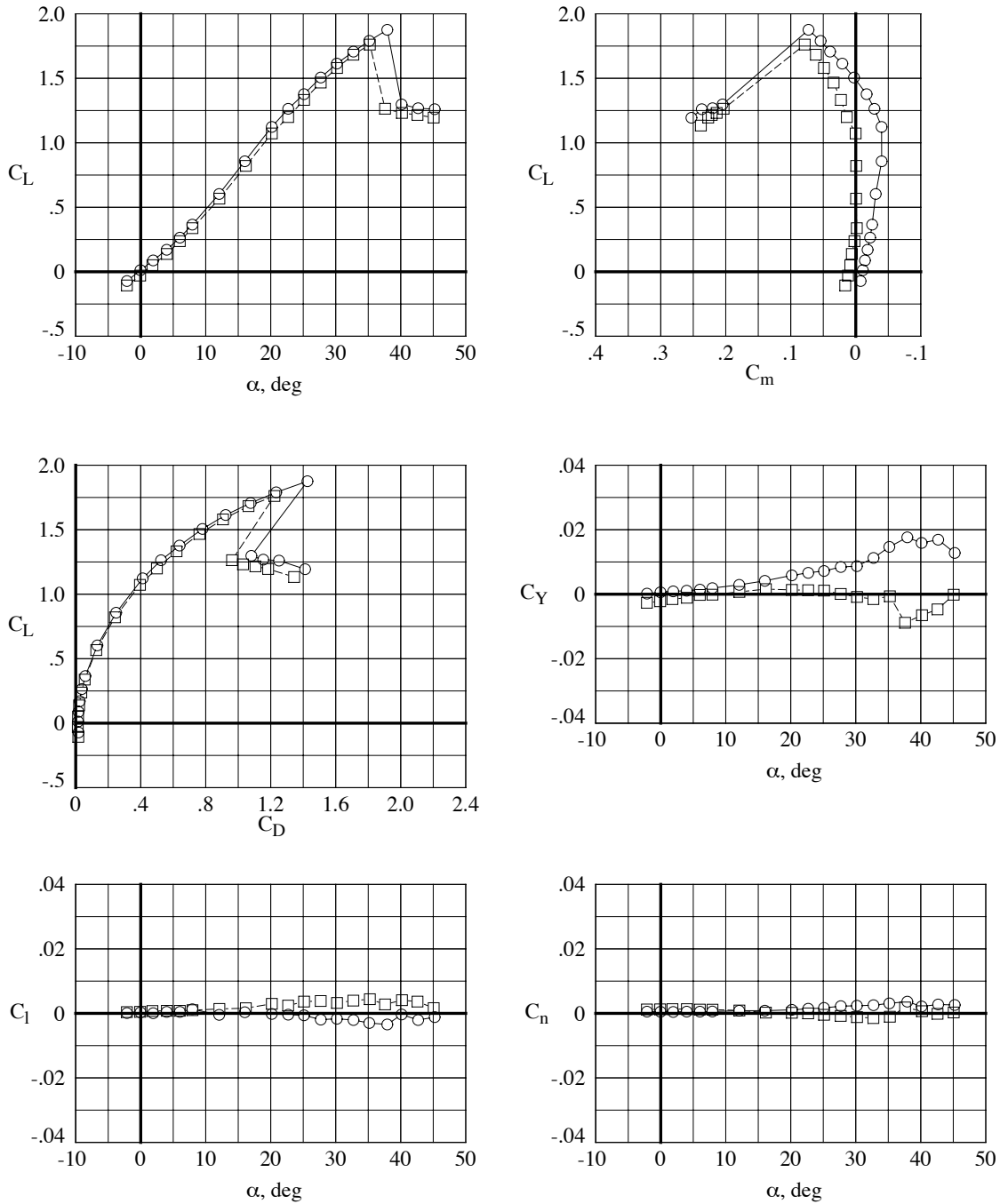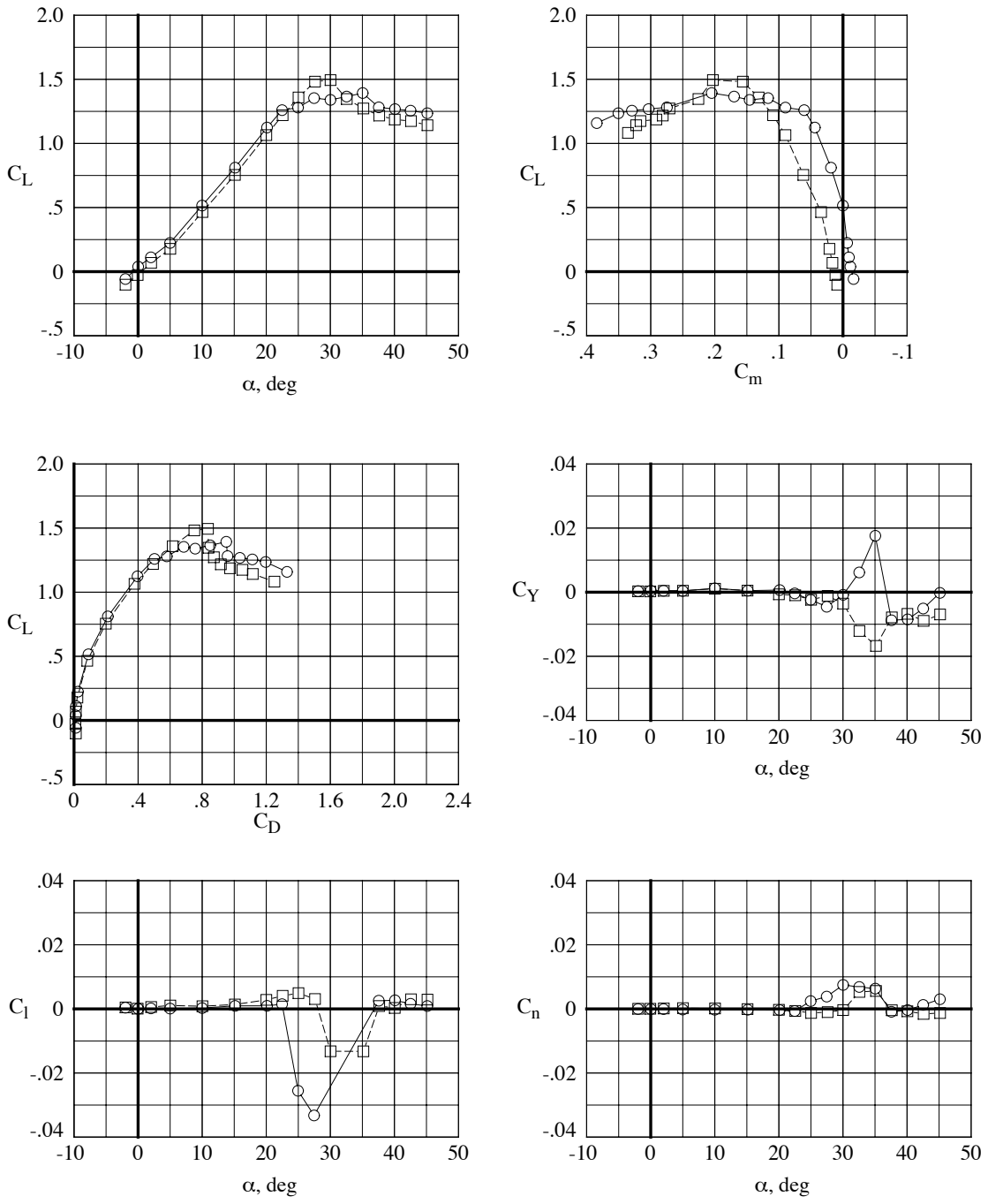| | Facility | Chine | Orientation | $M_\infty$ | $R_{\bar{c}}/10^6$ |
|---|---|---|---|---|---|
| ○——— | 7x10-Foot HST | 30. | Upright | 0.401 | 2.61 |
| □-------- | 7x10-Foot HST | 30. | Inverted | 0.401 | 2.84 |

Figure 5.  30° chine fuselage. Force and moment data for upright and inverted configurations. $\beta = 0°$.

7

| | Facility | Chine | Orientation | $M_\infty$ | $R_{\bar{c}}/10^6$ |
|---|---|---|---|---|---|
| ○——— | 7x10-Foot HST | 100. | Upright | 0.402 | 2.67 |
| □------ | 7x10-Foot HST | 100. | Inverted | 0.401 | 2.69 |

Figure 6.  100° chine fuselage. Force and moment data for upright and inverted configurations. $\beta = 0°$.

| | Facility | Chine | Orientation | $M_\infty$ | $R_{\bar{c}}/10^6$ |
|---|---|---|---|---|---|
| ○ | 7x10-Foot HST | 30. | Upright | 0.401 | 2.68 |
| □ | 7x10-Foot HST | 30. | Inverted | 0.401 | 2.84 |
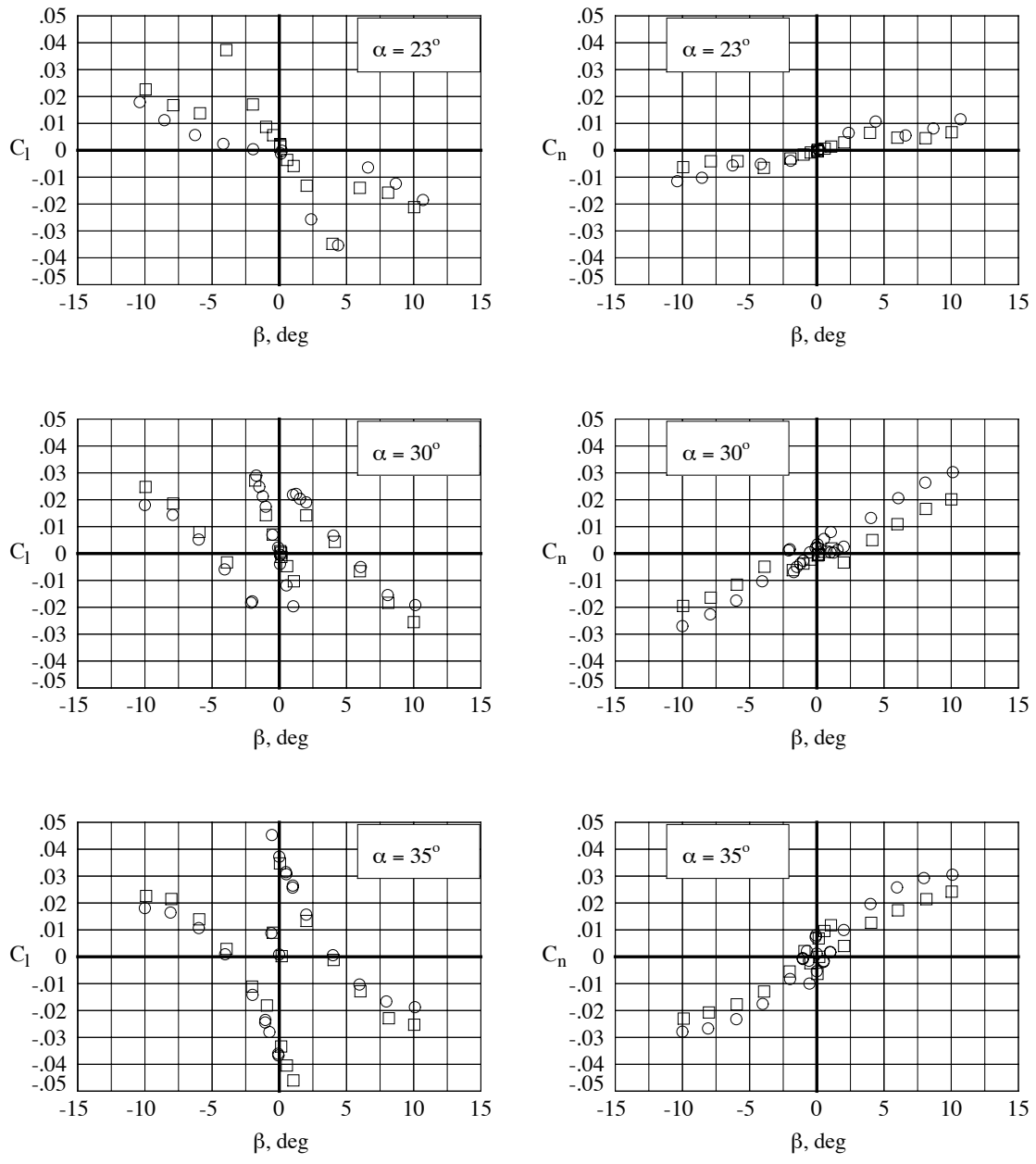


Figure 7. 30° chine fuselage. Rolling and yawing moment data for upright and inverted configurations.

| | Facility | Chine | Orientation | $M_\infty$ | $R_{\bar{c}}/10^6$ |
|---|---|---|---|---|---|
| ○ | 7x10-Foot HST | 100. | Upright | 0.402 | 2.65 |
| □ | 7x10-Foot HST | 100. | Inverted | 0.401 | 2.61 |
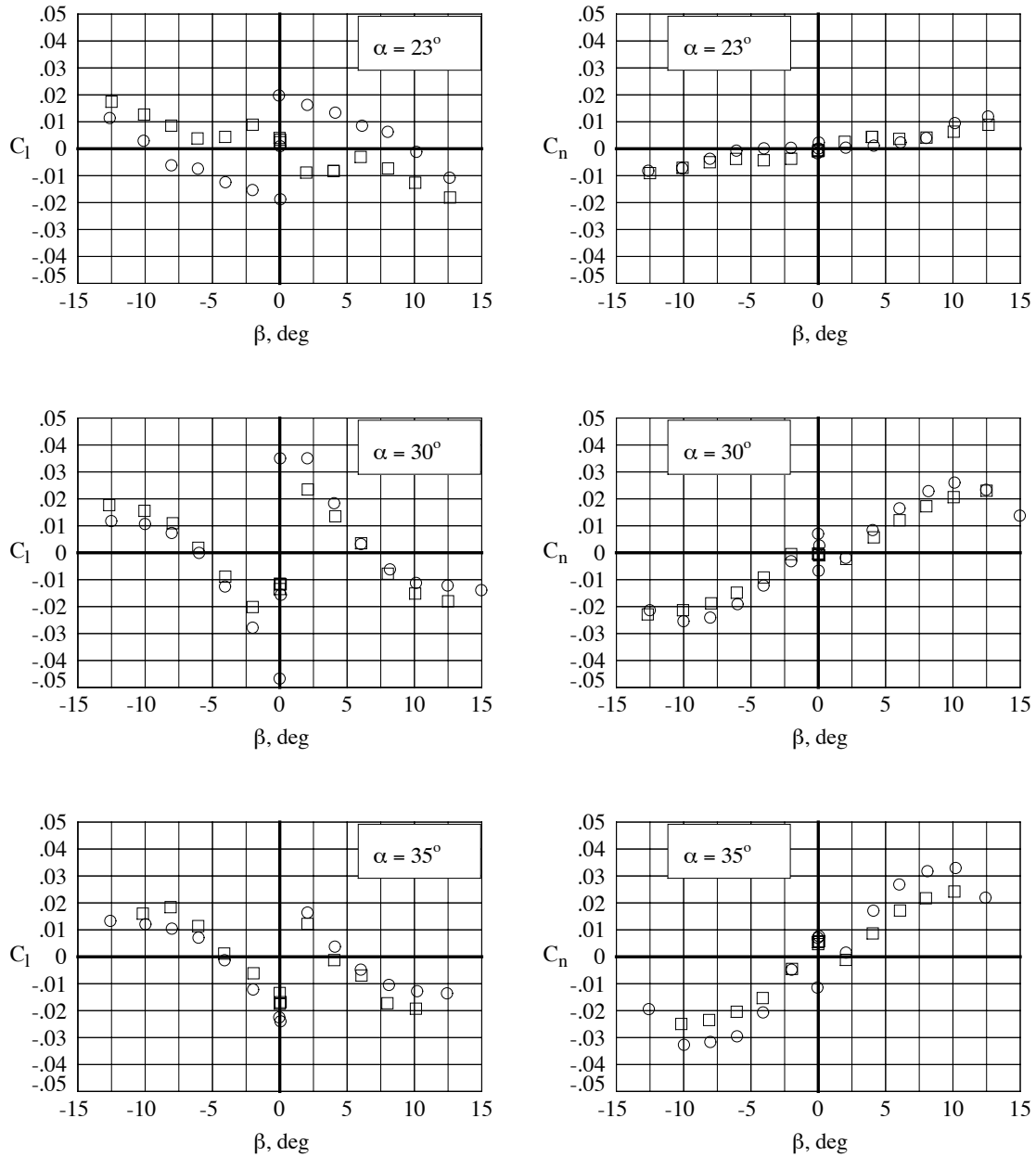


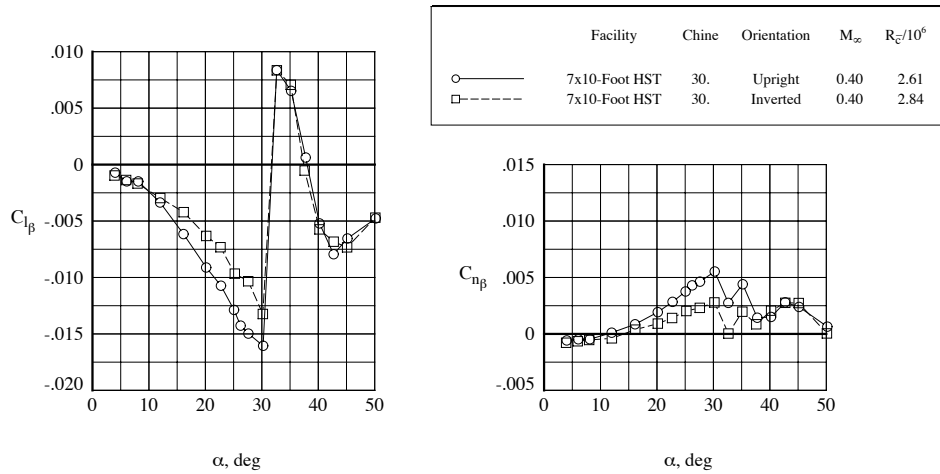Figure 8.  100$^o$ chine fuselage.  Rolling and yawing moment data for upright and inverted configurations.

Figure 9. 30° chine fuselage. Lateral/directional derivatives for upright and inverted configurations.
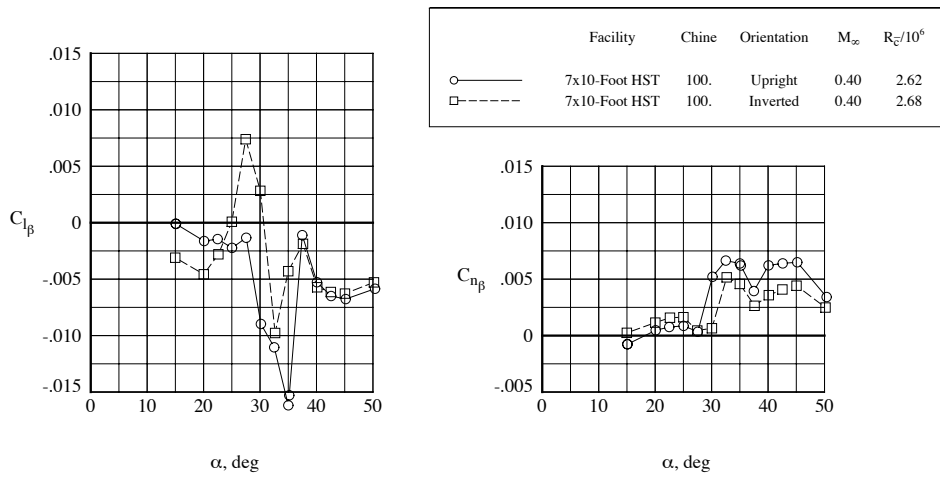


Figure 10. 100° chine fuselage. Lateral/directional derivatives for upright and inverted configurations.
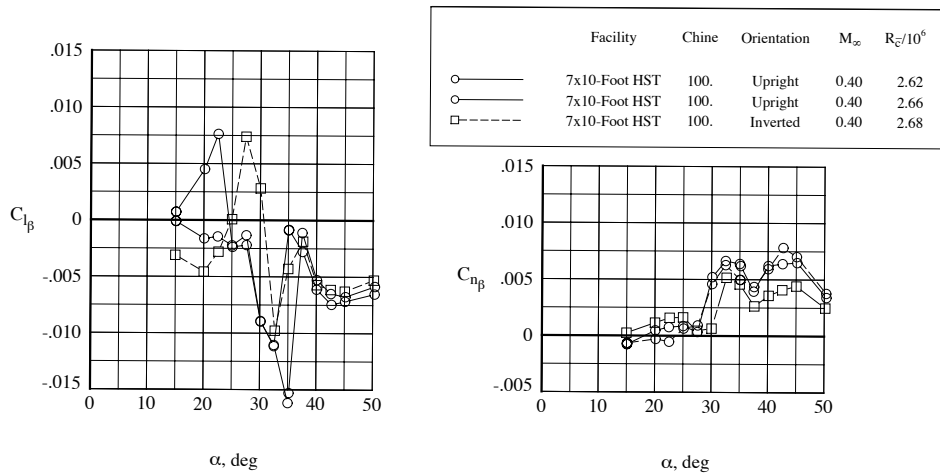


Figure 11. 100° chine fuselage. Lateral/directional derivatives with additional repeat information for upright configuration.

11

American Institute of Aeronautics and Astronautics